PCCP

PAPER

View Article Online
View Journal | View Issue

Cite this: *Phys. Chem. Chem. Phys.*, 2019, **21**, 20661

Ferroelectric nanocomposite networks with high energy storage capacitance and low ferroelectric loss by designing a hierarchical interface architecture†

Yingxin Chen,[a] Yifeng Yue,[a] Jie Liu,[c] Jie Shu,[e] Aiping Liu,[d] Baojin Chu,[c] Minhui Xu,[a] Weizhong Xu,[d] Tong Chen,[a] Jian Zhang *[a] and Qun-Dong Shen *[b]

Received 17th June 2019,
Accepted 23rd August 2019

DOI: 10.1039/c9cp03389k

rsc.li/pccp

Nanoscale design of nanofillers and interfacial architecture are vital to achieve high-capacity and high-energy-conversion efficiency poly(vinylidene fluoride) [(PVDF)-based] nanocomposite materials for vast potential applications in modern electronic devices and electric power systems. Using traditional methods, the addition of ceramic nanoparticles can only produce one type of interface between the nanoparticles and this matrix, achieving an enhanced dielectric constant and energy density at the expense of the charge–discharge efficiency. Herein, we demonstrate a novel class of cross-linking nanofiller system, poly(vinylidene fluoride-chlorotrifluoroethylene)/γ-methacryloylpropyl trimethoxysilane@$BaTiO_3$ [P(VDF-CTFE)/MPS@BT]. This novel approach can not only provide the interfaces between the nanoparticle and the matrix, but also scale down the size of crystalline domains, which results in producing more additional interfaces between the crystalline and amorphous phases to achieve an improved discharged energy density. Remarkably, the smaller crystalline domains, which were characterized by XRD and FTIR spectroscopy, could be beneficial for improving the dipole switchability from the polar phases to non-polar phases during the charge–discharge cycles, leading to unprecedented charge–discharge efficiency. Furthermore, the addition of MPS@BT NPs can regulate two stages of the discharge rate. The early discharge process can be accelerated, while the following stage is obviously delayed. The simplicity of the hierarchical interfacial engineering method provides a promising path to design ferroelectric polymer nanocomposites for dielectric capacitor applications.

Introduction

Electric energy is an indispensable and important resource in modern society. In power conversion and transmission systems, the exploitation of polymer-based capacitors with high-energy-density and low energy loss plays a very vital role in optimizing the use of electric energy storage and transmission, and enables large electric equipment to work under normal operating conditions.[1–5] Recently, dramatic improvements in the energy density of PVDF-based nanocomposite systems have been widely sought, as capacitors often occupy a vast majority of weight and volume of storage-conversion devices.[6,7] However, in order to replace commercial dielectric materials (biaxially oriented polypropylene),[8,9] dielectric/ferroelectric loss in PVDF-based nanocomposite systems is still a vital problem to be overcome.

The nanocomposite approach is one of the typical methods to introduce more interfaces between nanofillers and the matrix to attain a high energy density of PVDF-based polymers.[10,11] Firstly, ceramic nanoparticles, such as lead zirconate titanate (PZT),[12,13] barium titanate (BT),[14,15] or relaxor ferroelectrics,[16] which are often the most preferred high-dielectric-constant nanofillers, have been introduced into PVDF-based polymer matrices to further achieve high-energy-density ferroelectric nanocomposites. Unfortunately, the nanocomposite approach presents a series of new scientific issues, such as poor compatibility and problems with the interface between nanofillers and the associated matrices, resulting in a significant decrease in the breakdown strength and charge–discharge efficiencies. Furthermore, several new methods have therefore been devised

[a] *College of Materials & Environmental Engineering, Hangzhou Dianzi University, Hangzhou 310018, China. E-mail: jianzhang@hdu.edu.cn*
[b] *Key Laboratory of High Performance Polymer Materials and Technology of MOE, School of Chemistry & Chemical Engineering, Nanjing University, Nanjing, 210023, China. E-mail: qdshen@nju.edu.cn*
[c] *CAS Key Laboratory of Materials for Energy Conversion and Department of Materials Science and Engineering, University of Science and Technology of China, No. 96 Jinzhai Rd., Hefei, Anhui, 230026, China*
[d] *Center for Optoelectronics Materials and Devices, Zhejiang Sci-Tech University, Hangzhou, 310018, China*
[e] *Analysis and Testing Center, Soochow University, Suzhou, 215123, China*
† Electronic supplementary information (ESI) available. See DOI: 10.1039/c9cp03389k

to improve the compatibility and distributional homogeneity of these composites, including the synthesis of surface-functionalized nanofibers,[17,18] core–shell structure nanofillers,[19,20] and ternary polymer nanocomposites.[14] For instance, these new effective approaches include using high-dielectric constant nanofillers encapsulated by surface-modifying agents, molecular chains of polymers,[21] or insulating inorganic materials[22] to set up a new interface between the shell layer and the core layer, forming core–shell ceramic nanoparticles. Remarkably, the resulting shell layer is beneficial for stabilizing the nanofillers in the polymer matrices, decreasing the surface energy, and resulting in improvements in compatibility and distributional homogeneity. Meanwhile, the new interface between the shell layer and the core layer is favorable to store more charges, so such approaches can achieve simultaneous enhancements to dielectric constant (K) and energy density (U) in PVDF-based polymers. Due to the chemically inert nature of fluorinated polymers, the crystalline domains and the inner interfaces between the crystalline and amorphous phase still remain constant. Therefore, ferroelectric and dielectric loss, which yields significant waste heat, still occurs, and this is a tough problem that cannot be solved using a simple nanocomposite method.

On the other hand, modifications of the PVDF chemical structure, using methods such as copolymerization,[23,24] grafting,[25,26] and cross-linking,[18,27,28] are effective strategies for reducing highly-coupled dipole interactions and decreasing the size of large crystalline domains, resulting in high electric energy storage with low losses. For instance, compared with the homopolymer PVDF, some remarkable properties, such as higher energy densities and lower losses, have been obtained in poly(vinylidene fluoride-chlorotrifluoroethylene) [P(VDF-CTFE)] or poly(vinylidene fluoride-hexafluoropropene) [P(VDF-HFP)] copolymers due to the presence of the bulky CTFE/HFP units disrupting the sequence length of the crystal.[29,30] Moreover, cross-linking networks are predominately established in the P(VDF-HFP) chains, which allows the precise formation of these paraelectric crystals and enhances the reversibility of dipole switching in the crystalline phase, leading to the achievement of high energy density and low dielectric loss.[27] Thirdly, the use of grafted polyester polymers and polystyrene is another effective method for reducing the ferroelectric/dielectric loss of a matrix of P(VDF-CTFE), because PVDF lamellar crystals are encapsulated by a low polarizability interfacial layer to reduce compensation polarization during the dipole switching processes.[25] In a word, the improvement of energy density by the modifications of the PVDF chemical structure is not as obvious as that by the nanocomposite approach, but the cross-linking method can effectively reduce dielectric and ferroelectric loss in PVDF-based polymers.

Therefore, to overcome the disadvantages of these two strategies, a nanocomposite approach or one of modifying a PVDF chemical structure, we propose a new class of P(VDF-CTFE)/MPS@BT ferroelectric nanocomposite networks, which were prepared using a cross-linking method. In this method, BT nanoparticles were first surface-modified with a coupling agent, γ-methacryloylpropyltrimethoxysilane (MPS), and double bonds were then introduced onto the surface of these particles, forming double-bonded MPS@BT NPs. Next, the double-bond MPS@BT NPs and benzoyl peroxide (BPO) were successively added to the matrix P(VDF-CTFE) to form P(VDF-CTFE)/MPS@BT ferroelectric nanocomposite networks. In contrast to previous reports, double-bond-containing BT nanoparticles can not only tailor down crystalline domains to solve the critical issue of poor charge–discharge efficiency, but also set up hierarchical interfaces in the ferroelectric nanocomposite network system to achieve high energy density. Finally, surface molecular engineering in ceramic nanoparticles should help to tailor a unique class of ferroelectric nanocomposite materials for capacitor applications.

Results and discussion

In Fig. 1a, it can be seen that hydroxyl groups on the surface of BT NPs were activated by H_2O_2 treatment. Then, the resulting groups reacted with the silane coupling agent, γ-methacryloylpropyltrimethoxysilane (MPS), forming surface double bond-containing MPS@BT NPs.[31] On this basis, we hypothesized a new design for a nanofiller system using a one-pot cross-linking approach. Firstly, 5 wt%, 10 wt%, and 15 wt% MPS@BT NPs were mixed into P(VDF-CTFE) to form P(VDF-CTFE)/MPS@BT nanocomposites, which were defined as B_5, B_{10}, and B_{15}. Then, as shown in Fig. 1b, ferroelectric nanocomposite networks were fabricated by utilizing BPO as a cross-link initiator and using MPS@BT NPs as a cross-link center.[27] Variable mass fractions of BPO were added into the ferroelectric nanocomposite B_{10} and cross-linked at a high temperature of 200 °C to form nanocomposite networks, which were named nanocomposite networks $B_{10}P_5$, $B_{10}P_{10}$, $B_{10}P_{15}$, and $B_{10}P_{20}$, respectively.

Before the grafting of MPS, the edges of raw BT NPs were relatively smooth, as shown in Fig. 1c. The lattice fringes of BT NPs in the HR-TEM image (the inset) were found to be 0.40 nm, which is related to the (100) lattice spacing of tetragonal BT.[32] After grafting of the shell structure with MPS, the surfaces of the grafted particles (MPS@BT) became rough with clear irregularities (Fig. 1d), and this was caused by the coating of the grafted MPS. Fig. 1e compares the results of X-ray diffraction (XRD) analysis of BT NPs and MPS@BT NPs, which suggests that all the characteristic peaks are in good agreement with tetragonal BT, and the shell layer cannot change the crystalline structure.[33] However, the decreased intensity of BT was related to the existence of the MPS layer shell. As shown in Fig. 1f, when the heating temperature rose to 660 °C, the weight loss of the raw BT NPs and MPS@BT grafted nanoparticles was 99.74% and 97.2%, respectively. The difference in the weight loss between raw BT NPs and MPS@BT NPs was in the weight of the grafted MPS on the surfaces of BT NPs. The grafting degree of MPS@BT NPs was about 2.56 g/100 g. In a word, double-bonds in MPS were successfully synthesized on the surface of BT NPs.

Furthermore, more details of the mechanism of the cross-linking reaction are shown in Fig. S1 (ESI†). BPO produces highly reactive radicals at 200 °C upon heating (Fig. S1a, ESI†). Double bonds on the surface of BT NPs (Fig. S1b, ESI†), chlorine atoms in CTFE monomer units, and hydrogen atoms (Fig. S1c, ESI†) were

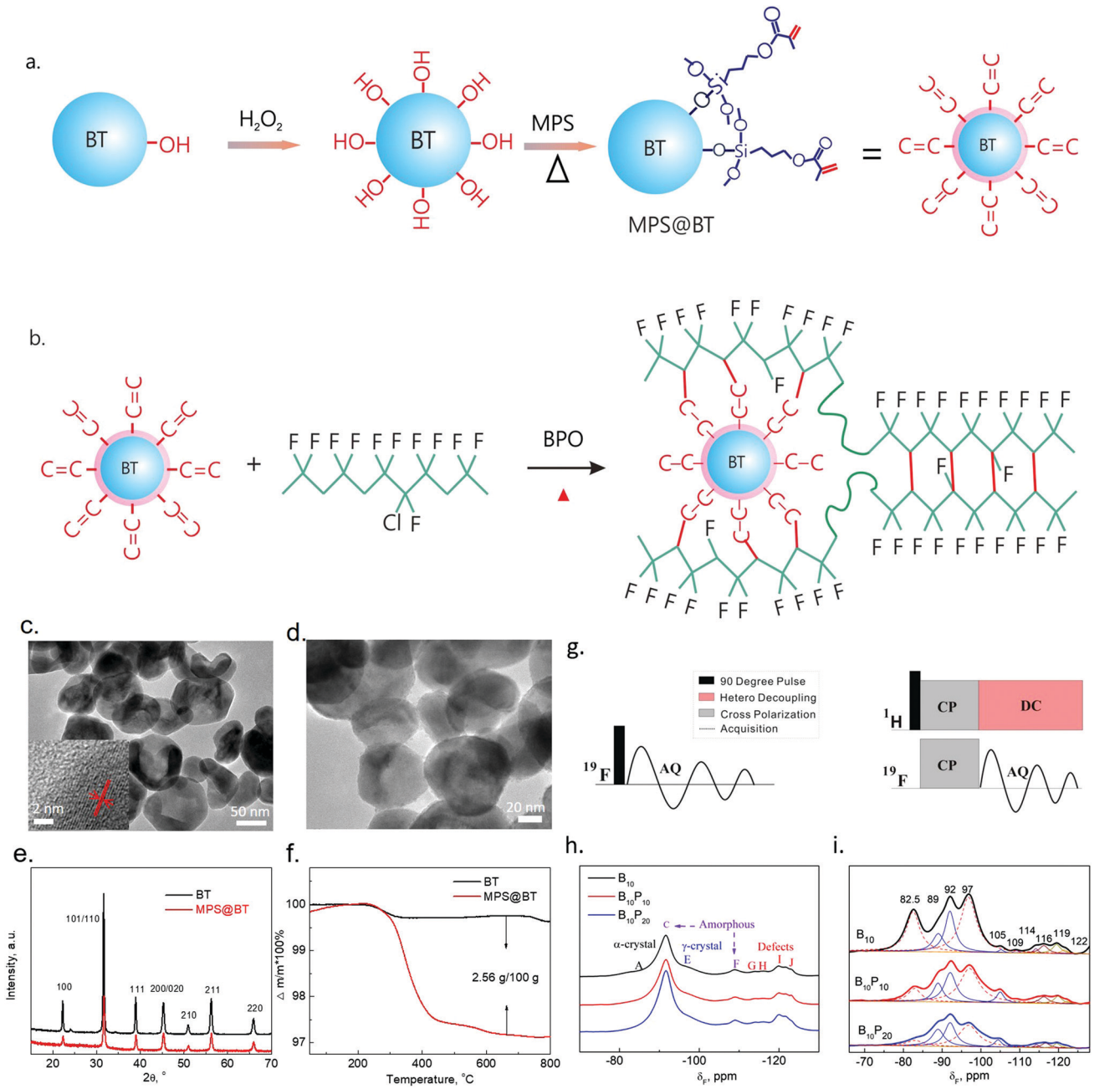

Fig. 1 (a) Schematic illustration of double-bond MPS@BT particles, and the double bonds are fixed on the surface by a chemical bond; (b) the cross-linking reactions in P(VDF-CTFE)/MPS@BT nanocomposite networks. (c) TEM image and high-resolution (HR)-TEM image (insets) of raw BT NPs, (d) TEM image of MPS@BT NPs, (e) room-temperature X-ray diffraction patterns of BT NPs and MPS@BT NPs, and (f) TGA curves for raw BT and double-bond MPS@BT NPs. (g) Pulse sequences of ^{19}F direct polarization (DP) and ^{19}F{^{1}H} cross polarization (CP) experiments for selective observation in the crystalline phase. (h) ^{19}F DP and (i) ^{19}F{^{1}H} CP NMR spectra of the nanocomposites (B_{10}), and the nanocomposite networks ($B_{10}P_{10}$ and $B_{10}P_{20}$); crystalline components recorded with a CP contact time of 50 μs and a magic angle spinning frequency of 18 kHz. The spectra were deconvoluted by using ten Lorentzian functions.

readily depleted by these radicals to produce macromolecular radicals, which finally evolved into a cross-linked network (Fig. S1d, ESI†). The above mechanism of the cross-linking reaction was identified by the solid-state ^{19}F-NMR results. Fig. 1g exhibits the specific methods to determine the structure by pulse sequences of ^{19}F direct polarization (DP) and ^{19}F{^{1}H}. Fig. 1h shows the corresponding ^{19}F NMR DP spectra of the nanocomposite networks (B_{10}, $B_{10}P_{10}$, and $B_{10}P_{20}$). The intensity of VDF group in the amorphous phase at −82 ppm and −109 ppm was enhanced with the increasing content of BPO. Interestingly, ^{1}H → ^{19}F CP experiments were performed and only crystalline phase signals were detected in the very short CP contact time of 50 μs, as shown in Fig. 1i. The intensity of the α-form crystals at −82.5 and −97 ppm and the γ-form crystals at −89, −92, −105,

and −109 ppm obviously decreased. Meanwhile, region-irregular structures (−104, −106, −108 and −122 ppm) were found in CP experiments, indicating that CTFE units are included in the crystals and are able to participate in the crystalline form.[36] The decreased intensity is related to the occurrence of the dehydrochlorination reaction and the crosslinking points forming in the CTFE group. Taken together, this indicates that the cross-linking points were mainly established in the VDF and CTFE units of the crystalline phase region, resulting in tailoring down α and γ form crystals and generating more amorphous phase in the nanocomposite networks.

The cross-sectional morphology of P(VDF-CTFE)/BT nanocomposites and P(VDF-CTFE)/MPS@BT nanocomposites is shown in Fig. 2a and b, respectively. Comparatively, considerable nanoparticle aggregation and a large number of micropores have been found in the P(VDF-CTFE)/BT nanocomposite system. However, MPS@BT NPs were well-separated and uniformly distributed in the cross-linked P(VDF-CTFE), possibly due to the high interfacial adhesion of the MPS shell structure to the surface of BT NPs.

The crystalline phases of P(VDF-CTFE)/MPS@BT nanocomposites and nanocomposite networks were studied by recording their XRD pattern and FTIR spectrum, as shown in Fig. 2c and Fig. S2 (ESI†), respectively. P(VDF-CTFE) copolymer shows three peaks at 16.4°, 17.8°, and 19.9°, which could be assigned to the (100), (020), and (110) reflections of the paraelectric crystalline α-phase, respectively.[7] With an increase in the MPS@BT content, the nanocomposites (B_5, B_{10}, and B_{15}) exhibited a growing diffraction peak around 20.8° (d = 4.25 Å), which could be related to the β-phase of VDF sequences. Consequently, the intensity of the peaks at 16.4°, 17.8°, and 19.9° reduced, indicating that the partial nonpolar crystalline α-phase was converted into a polar crystalline β-phase. However, the opposite effect occurred in the polymorphic crystalline phases of P(VDF-CTFE)/MPS@BT nanocomposite networks. With increasing addition of BPO content, the intensity of the shoulder at 20.8° was reduced, while the shoulders at 16.4°, 17.8°, and 19.9° were enhanced. Moreover, comparison of the FTIR spectra demonstrated that the chain conformation of the nanocomposites formed β polar phases upon the addition of MPS@BT and then generated non-polar α-phases upon cross-linking (Fig. S2, ESI†), which was consistent with the XRD results. The characteristic absorption bands at 1284 and 843 cm^{-1}, which were ascribed to $T_{>=4}G$ and $T_{>=3}G$ conformations of the crystalline β- or γ-phase, become more dominant with the addition of MPS@BT content.[33] Subsequently, the P(VDF-CTFE)/MPS@BT nanocomposite networks showed the opposite effect on polymorphic crystalline phases with increasing addition of BPO content. The intensity of the bands at 1284 and

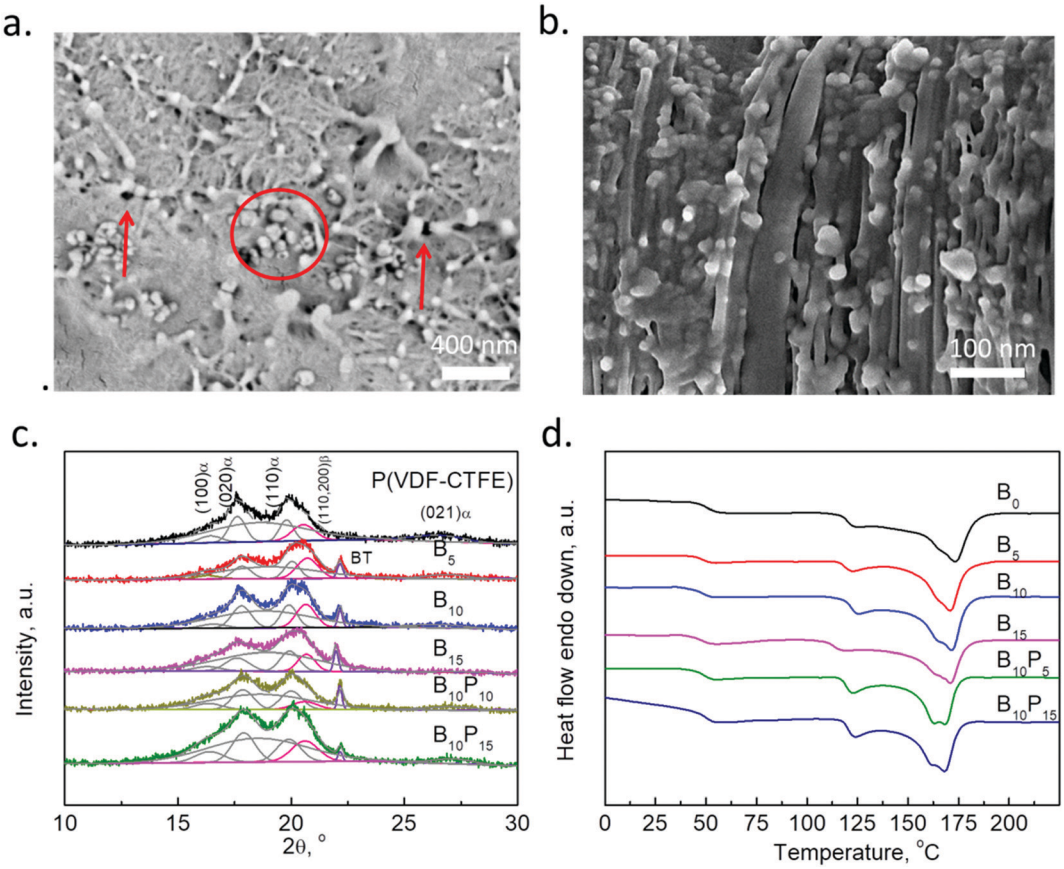

Fig. 2 Cross-sectional SEM images of (a) P(VDF-CTFE)/BT nanocomposites and (b) P(VDF-CTFE)/MPS@BT nanocomposite. (c) X-ray diffraction (XRD) curves; the curves are well fitted by Gaussian. (d) DSC curves of P(VDF-CTFE)/MPS@BT nanocomposites (B_0, B_5, B_{10}, and B_{15}) and P(VDF-CTFE)/MPS@BT nanocomposite networks ($B_{10}P_{10}$, and $B_{10}P_{15}$).

843 cm^{-1} reduced with the increasing addition of BPO content, which was consistent with the results of XRD curves.

Furthermore, additional structural data of the P(VDF-CTFE)/MPS@BT nanocomposites and nanocomposite networks are summarized in Table S1 (ESI†). The mean size of the crystalline domains (L) for the (020) and (110, 200) faces in the nanocomposites and nanocomposite networks was calculated. This calculation is based on the Scherrer equation,[34] which can be written as:

$$L = \frac{0.9\lambda}{B\cos\theta} \quad (1)$$

where λ is the X-ray wavelength, L is the mean size of the crystalline domains, θ is the Bragg angle and B is the line broadening at half the maximum intensity (FWHM). With the increasing content of MPS@BT NPs, the α-phase crystallite size of P(VDF-CTFE) decreases. For instance, the size of α-phase in pristine P(VDF-CTFE) is about 11.0 nm, larger than that of the P(VDF-CTFE)/MPS@BT nanocomposites (B_5: 10.3 nm, B_{10}: 9.7 nm, and B_{15}: 8.1 nm). It is reasonable that MPS@BT NPs served as heterogeneous nucleation sites and led to a reduction in the nucleation barrier of these NPs. This is very beneficial to forming tiny spherulites on the surface of the MPS@BT NPs. In contrast, the size of the ferroelectric β-phase crystals grew from 6.7 to 9.0 nm with an increase in the MPS@BT content, as shown in Table S1 (ESI†). Furthermore, the α-phase and β-phase crystalline sizes simultaneously decreased when the cross-linking networks were established in the nanocomposite. For instance, the size of the ferroelectric β-phase crystals decreased from 8.1 to 5.8 nm with increasing addition of BPO content from 0–15%. As shown in Fig. 2d, with the increasing addition of MPS@BT content, the melting temperature of the nanocomposites (B_5, B_{10}, and B_{15}) shifted towards lower temperatures, indicating the formation of smaller crystalline domains. However, the relative crystallinity increased from 23.6 to 26.1%, as shown in Table S2 (ESI†). It is worth mentioning that the decrease in crystalline size did not lead to reducing crystallinity due to the increase in the number of nucleation centers associated with the presence of MPS@BT fillers. Furthermore, in contrast to nanocomposite B_{10}, the melting temperature of nanocomposite networks ($B_{10}P_{10}$, and $B_{10}P_{15}$) dropped to a lower temperature, and the relative crystallinity decreased as well.

Dielectric constant

The dielectric properties of P(VDF-CTFE)/MPS@BT nanocomposites with various MPS@BT NP contents are shown in Fig. 3a. As expected, the dielectric constant enhanced rapidly with an increase in the MPS@BT NP content. For instance, a relative permittivity of 129 at 1 kHz was attained in the P(VDF-CTFE)/MPS@BT nanocomposite, which was about 10 times greater than that of P(VDF-CTFE) copolymer (which was 13.7 at 1 kHz), indicating that the introduction of double-bond MPS@BT NPs was beneficial for improving the dielectric permittivity of the PVDF-based nanocomposite system. Another reason for obtaining a high dielectric permittivity was that new interfacial areas are naturally generated, thus more charges were built into the interfaces between MPS@BT NPs and P(VDF-CTFE).

To further improve dielectric permittivity, the cross-linking approach was optimized to modify the additional interfaces between crystalline and amorphous phases. Nanocomposite networks were prepared by the cross-linking method, which is composed of P(VDF-CTFE) as the matrix, benzoyl peroxide (BPO) as an initiator, and the double-bond MPS@BT NPs as cross-linking centers. Furthermore, the effects of the cross-linking agent on dielectric properties of P(VDF-CTFE)/MPS@BT nanocomposite networks are shown in Fig. 3b. It is clear that the addition of a cross-linking agent to a nanocomposite system had a huge effect on the dielectric constant. With the increase in the BPO content from 0% to 15%, the corresponding dielectric permittivity rose from 60.4 to 130. The enhanced dielectric constant is closely related to the fact that the α-phase and β-phase crystalline sizes simultaneously decreased when the cross-linking networks were established in the nanocomposite, and more additional interfaces between the crystalline and amorphous phases were produced. For instance, the ferroelectric β-phase crystalline size was decreased from 8.1 to 5.8 nm,

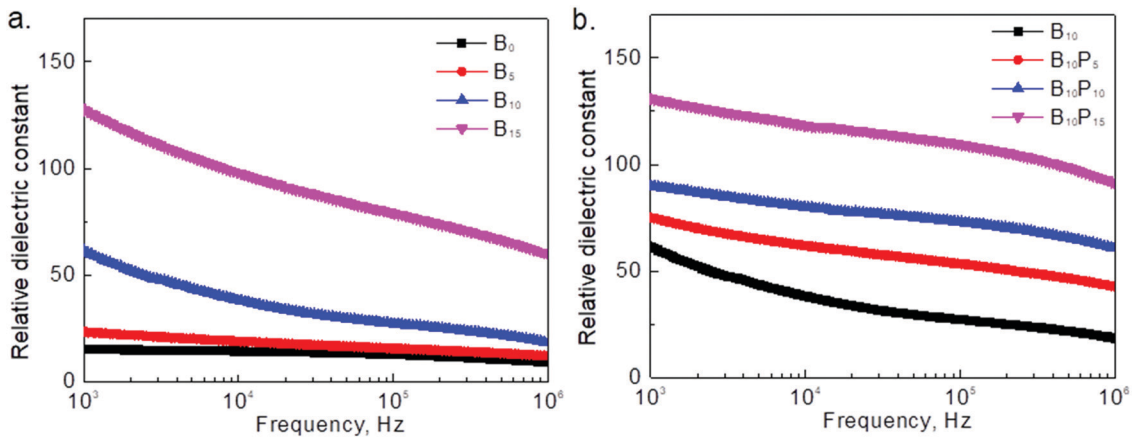

Fig. 3 (a) The variation of relative permittivity with room temperature at variable frequency from 10^3 to 10^6 in the P(VDF-CTFE)/MPS@BT nanocomposites B_0, B_5, B_{10} and B_{15}, and (b) P(VDF-CTFE)/MPS@BT nanocomposite networks B_{10}, $B_{10}P_5$, $B_{10}P_{10}$, and $B_{10}P_{15}$.

and paraelectric α-phase crystalline size was tailored down from 11.0 to 6.5 nm with increasing addition of BPO content from 0 to 15%, as shown in Fig. 2a and Table S1 (ESI†). Besides, in contrast to pristine P(VDF-CTFE), nanocomposite networks exhibited a lower melting temperature and a reduced crystallinity (Fig. 2d and Table S2, ESI†), which also indicates that the cross-linking method can tailor down the size of crystalline domains.

Energy storage at high electric field

The effects of surface-modified MPS@BT NPs on the high-field energy storage behavior of these polymer nanocomposites were then investigated. The *P*–*E* loops of these nanocomposites were compared up to 160 MV m^{-1} and the breakdown strength is shown in Fig. 4a. At the same electric fields, the nanocomposites showed a continuous increase in electric polarization. The increment depended strongly on the content of MPS@BT NPs. For example, when the electric field was 160 MV m^{-1}, the electric polarization of P(VDF-CTFE) copolymer was only 1.73 μC cm^{-2}, while that of the nanocomposites B_{10} and B_{15} was 2.98 and 3.90 μC cm^{-2}, respectively, demonstrating a 72% and 125% increase, respectively. Although the electric polarization was significantly improved, the corresponding remnant polarization also increased. For example, when the applied electric field was reduced to 0 MV m^{-1}, the remnant polarization of P(VDF-CTFE) copolymer was relatively low, only about 0.18 μC cm^{-2}. However, the P(VDF-CTFE)/MPS@BT nanocomposite had the highest remnant polarization at about 1.16 μC cm^{-2}, which was unfavorable for an increase in the discharged energy density and charge–discharge efficiency. The enhanced remnant polarization was closely related to the

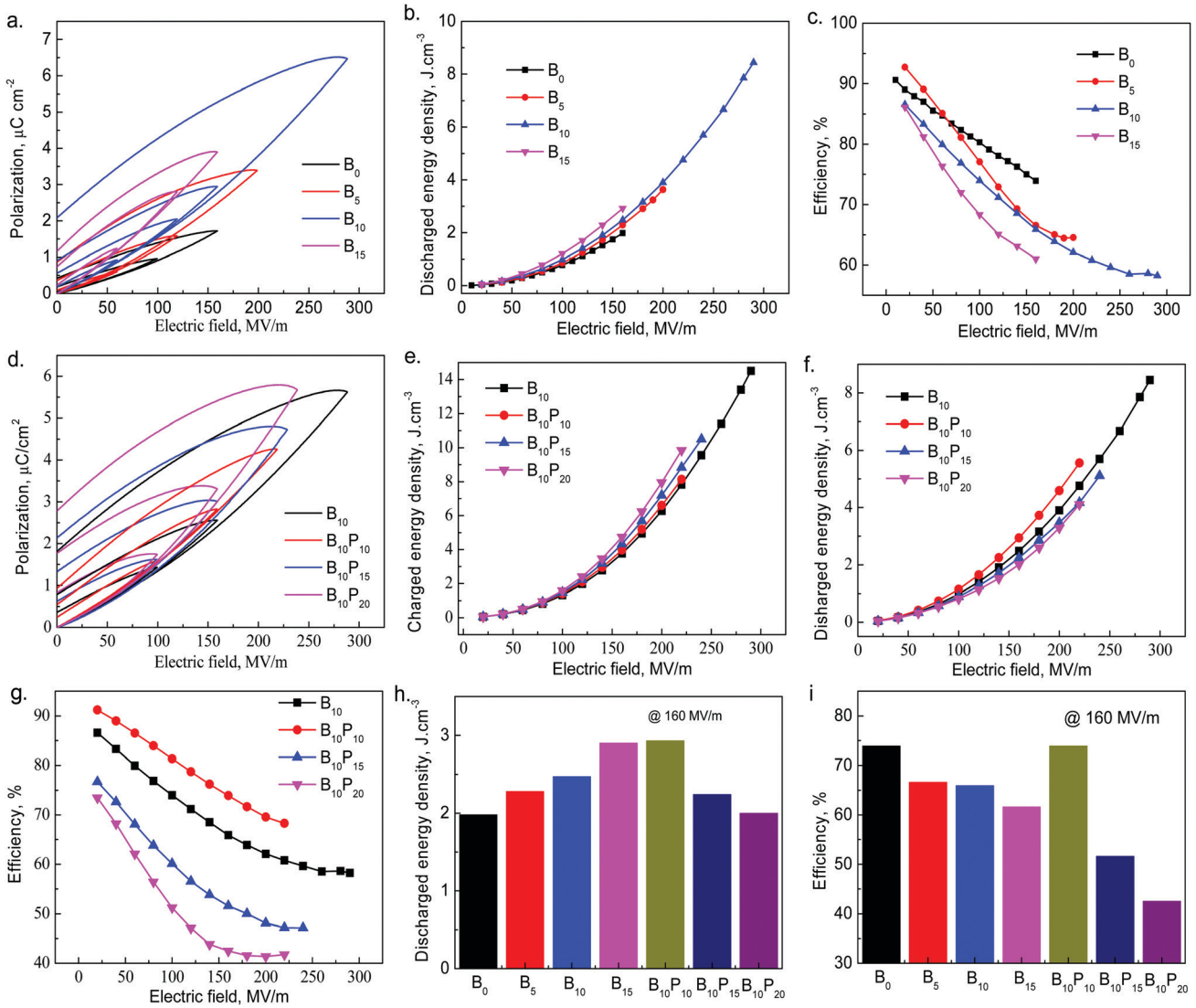

Fig. 4 (a) Polarization–electric field (*P*–*E*) loops, (b) discharged energy density, and (c) charge–discharge efficiency of P(VDF-CTFE)/MPS@BT nanocomposites with different contents of MPS@BT (B_0, B_5, B_{10}, and B_{15}) at different electric fields. (d) *P*–*E* loops, (e) charged energy density, (f) discharged energy density, and (g) charge–discharge efficiency of P(VDF-CTFE)/MPS@BT nanocomposite networks with different contents of BPO (B_{10}, $B_{10}P_{10}$, $B_{10}P_{15}$, and $B_{10}P_{20}$) at different electric fields. (h) Discharged energy density and (i) charge–discharge efficiency of B_0, B_5, B_{10}, B_{15}, $B_{10}P_{10}$, $B_{10}P_{15}$, and $B_{10}P_{20}$ under the electric field of 160 MV m^{-1}.

ferroelectric phase, which had all trans conformations in ferroelectric nanocomposites, as evidenced by the FTIR spectrum in Fig. S2 (ESI†).

For a dielectric capacitor, the value of energy density (U) is measured from the P–E loops using the integral $U = \int E\mathrm{d}D$.[34] The discharged/charged energy densities of the nanocomposites at different electric field are summarized and depicted in Fig. S3 (ESI†) and Fig. 4b. The corresponding charge–discharge efficiency at different electric field strengths can be calculated by the equation $\eta = \frac{U_{\text{discharged}}}{U_{\text{charged}}} \times 100\%$. With an increase in the electric field strength, the electric polarization of the ferroelectric nanocomposite reaches a maximum value, meaning the storage of electric energy, while a steady decrease in the field strength results in electric energy discharging from these dielectric materials. As expected, discharged energy density from the nanocomposite increased with a continuous increase of MPS@BT content in the same electric field (Fig. 4b). This was mainly due to the high dielectric constant of MPS@BT and the additional interfaces between MPS@BT and the matrix. However, adding more MPS@BT content to the matrix had negative effects on the charge–discharge efficiency, as shown in Fig. 4c. For instance, with the increasing content of MPS@BT from 5% to 15%, the corresponding charge–discharge efficiency reduced from 73.9 to 61.6, which shows an obvious decline in efficiency. The decreased efficiency was closely related to the fact that an increased ferroelectric phase with $T_{n>=4}G$ conformations was created in the P(VDF-CTFE)/MPS@BT nanocomposites. The other reason may be the fact that high loading of MPS@BT leads to more defects and voids in the ferroelectric nanocomposites, and the accumulated charges on the interfaces between MPS@BT and the P(VDF-HFP) matrix enhanced the interfacial polarization, thus, much of the stored energy was lost.

To solve the low charge–discharge efficiency problem and to also attain a high energy density at the same time, we developed a one-pot cross-linking approach to modify hierarchical interfaces in the P(VDF-CTFE)/MPS@BT nanocomposite networks. Unipolar P–E hysteresis loops of the nanocomposite networks ($B_{10}P_{10}$, $B_{10}P_{15}$, and $B_{10}P_{20}$) were characterized and compared in the same electric field (160 MV m^{-1}), and up to a maximal electric field, as shown in Fig. 4d. Unipolar P–E hysteresis loops of each sample in different electric fields are shown in Fig. S4 (ESI†). In comparison to nanocomposite B_{10}, the maximum polarization of the nanocomposite networks further increased with increasing content of double-bonded MPS@BT. The enhanced polarization may have been related to the surface double-bonds found in MPS@BT NPs, which served as cross-linking centers, not only creating more interfaces between MPS@BT and P(VDF-CTFE), but also producing more additional interfaces between crystalline and amorphous phases by decreasing the size of crystalline domains. The results of these unipolar P–E loops are consistent with the dielectric spectra. Therefore, the corresponding charged energy density was also improved, as shown in Fig. 4e. For instance, although the charged energy density of nanocomposite B_{10} was 7.8 J cm^{-3}, the nanocomposite network of $B_{10}P_{20}$ shows an unprecedented energy density of 9.8 J cm^{-3}, exhibiting a 26% increase. Interestingly, discharged energy density and the charge–discharge efficiency of nanocomposite networks first increase, and then reduce with increasing content of BPO, as shown in Fig. 4f and h, respectively. Consequently, high discharged energy densities and a high charge–discharge efficiency were attained in P(VDF-CTFE)/MPS@BT nanocomposite networks using this cross-linking method. For example, at a low electric field of 160 MV m^{-1}, a discharged energy density of around 2.9 J cm^{-3} was achieved in the $B_{10}P_{10}$ films, and this was almost 1.5 times that of the P(VDF-CTFE) films with a discharged energy density of 2.0 J cm^{-3}, as shown in Fig. 4i. Typically, the charge–discharge efficiency is kept constant, and this value was 74% in both P(VDF-CTFE) and ferroelectric nanocomposite networks of $B_{10}P_{10}$ (Fig. 4j). Therefore, the double-bond MPS@BT NPs play a dual role in the ferroelectric nanocomposite networks. First, the surface double-bonds in the MPS@BT NPs, which only serve as high-dielectric-constant nanoparticles, generate more interfaces between the nanoparticles and the matrix to enhance the K values and the discharge energy density. However, the shortcoming of this nanocomposite approach is that P(VDF-CTFE)/MPS@BT nanocomposites exhibit poor charge–discharge efficiency when the loading content is high. Furthermore, the surface double-bonds of MPS@BT NPs, which are introduced in cross-linked networks by the cross-linked method, can further decrease the size of crystalline domains, thus producing additional interfaces between crystalline and amorphous phases for achieving improved charge–discharge efficiency and discharged energy density.

Fast discharge rate

In order to illustrate the ultra-fast discharge rate of these nanocomposite networks and thus their high power densities, a classic fast-discharge system is described in Fig. 5a, in which the discharged energy was determined using a load resistor R_L in series.[6,35] The representative discharge profiles from a series of resistor loads are shown in Fig. 5b. The discharge time is the time when the discharge energy reaches 95% of the final value in a load resistor. For the P(VDF-CTFE) capacitor discharging to a 10 kΩ, 100 kΩ, and 3 MΩ load, the energy discharge time was about 1.5 μs, 48 μs, and 1965 μs, respectively. This indicates that the discharge time can be deduced from R_LC (where C is the capacitance), and is also controlled by the external load resistor R_L. Furthermore, with an increase in the electric field from 50 MV m^{-1} to 110 MV m^{-1}, the discharge time increased from 34 μs to 44 μs (Fig. 5c), and the corresponding energy density increased from 0.09 J cm^{-3} (at a power density of 2.6 × 10^{-3} MW cm^{-3}) to 0.47 J cm^{-3} (at a power density of 1.1 × 10^{-2} MW cm^{-3}), indicating that the energy density increased by the square of the field strength. Finally, a comparison of discharge dynamics between P(VDF-CTFE) and the nanocomposite networks at a fixed electric field of 80 MV m^{-1} was performed (Fig. 5d). We found that P(VDF-CTFE)/MPS@BT nanocomposite networks released their energy density at a rate of microseconds. For example, discharge took 80 μs for $B_{10}P_{10}$, comparable to pristine films, which have a discharging time of 40 μs. In the same electric field of 80 MV m^{-1}, the discharged energy density

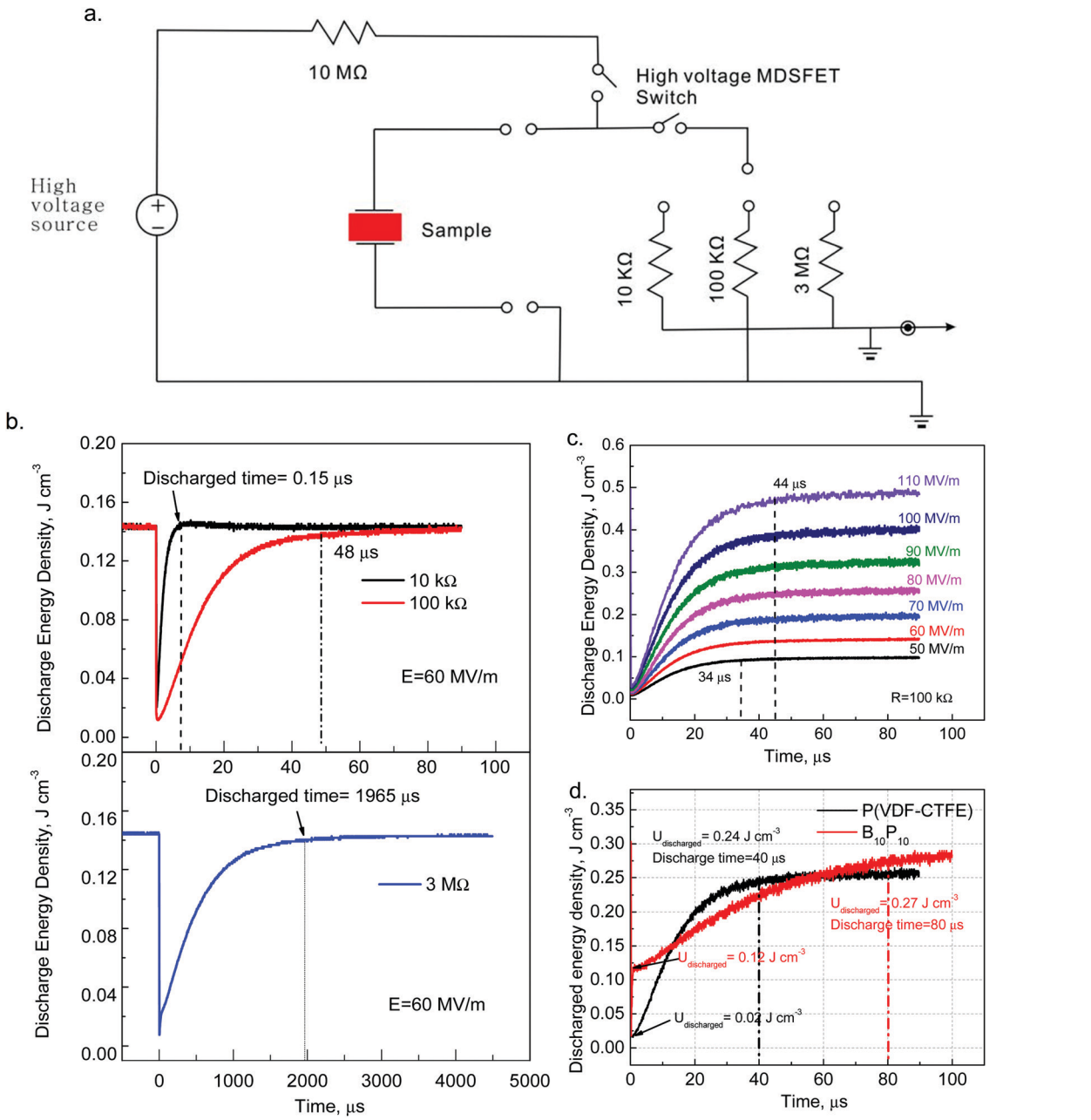

Fig. 5 (a) Discharge circuit for energy density and discharge speed characterization. Discharged energy density *versus* the discharge time for P(VDF-CTFE) (b) with 10 kΩ, 100 kΩ, and 3 MΩ load resistor and (c) under the electric field varied from 50 MV m^{-1} to 110 MV m^{-1}. (d) Discharged energy density *versus* the discharge time for P(VDF-CTFE) and nanocomposite networks of $B_{10}P_{10}$ with the 100 kΩ load resistor in the electric field of 80 MV m^{-1}.

of nanocomposite networks was about 0.27 J cm^{-3}, which was 1.12 times higher than that of P(VDF-CTFE). Furthermore, two discharge stages are found in the nanocomposite networks. In the early stage of the discharge process, the energy release rate of nanocomposite networks was much faster than that of the matrix. For instance, when the discharge time was about 1 μs, the discharged energy density of $B_{10}P_{10}$ was about 1.2 J cm^{-3}, which was 6 times higher than that of P(VDF-CTFE). This demonstrates that the acceleration of the early discharge process may be closely related to the MPS@BT NPs, which are a ceramic dielectric material with a short polarization-retention time. In the following stage of the discharge process, the energy discharge rate of the nanocomposite networks slows down, and it is significantly lower than that of P(VDF-CTFE). This slow discharge process can be mainly attributed to the fact that setting up networks in a nanocomposite can decrease the size of crystalline domains, and crystalline domains are trapped in the amorphous phase. Thus, the addition of the novel nanofiller MPS@BT NPs not only improves discharged energy density, but also regulates energy discharge rate. All of these excellent features make ferroelectric nanocomposite networks a promising candidate for compact and flexible high-power capacitors.

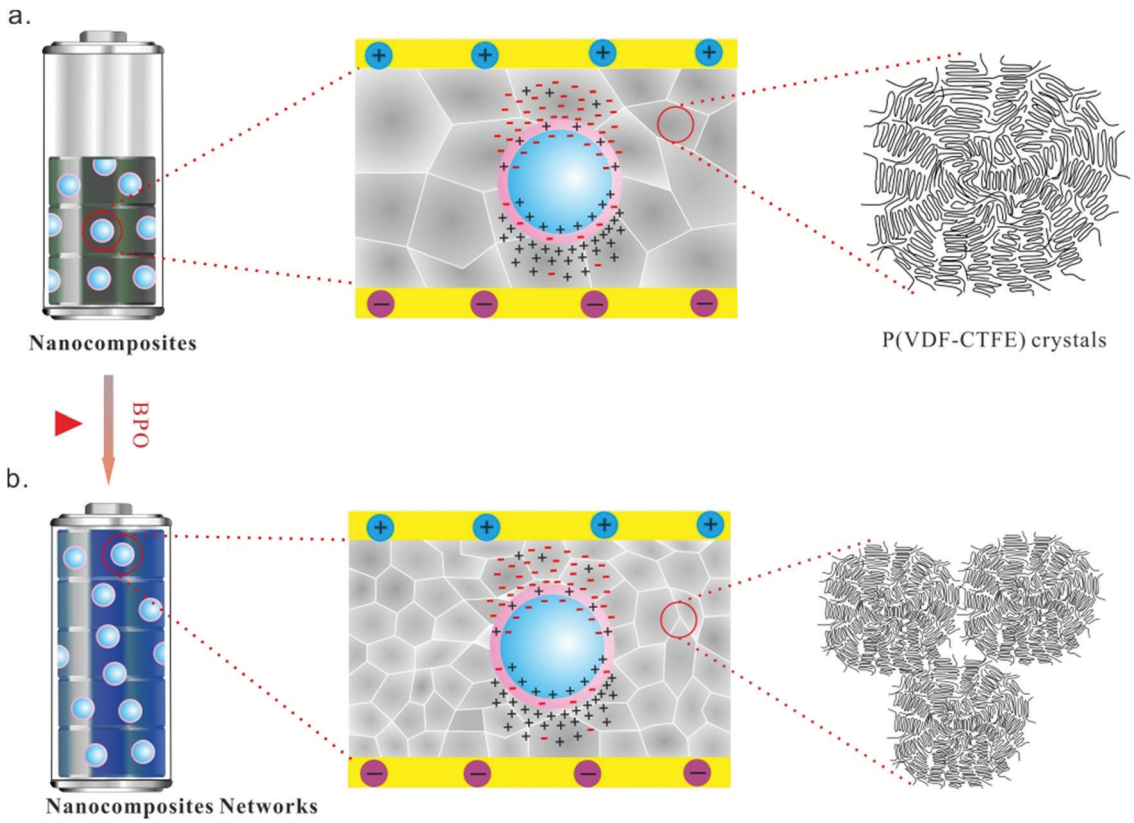

Fig. 6 Schematic illustration of the relationship between energy density and hierarchical interface: (a) P(VDF-CTFE)/MPS@BT nanocomposite and (b) nanocomposite networks with hierarchical interfaces and their crystals.

The mechanism of the novel BT@MPS nanofiller in improved dielectric performance

We present a new design for a nanofiller system with low ferroelectric loss and high energy density using the cross-linking approach. The relationship between energy density and hierarchical interfaces is found as below: firstly, the addition of BT@MPS produced an interface between the nanoparticles and the matrix, which results in the improvement of dielectric constant along with the energy density. Besides, improving the interfacial polarization, as well as enabling more space charge accumulation at the hierarchical interface, is favorable for improving the dielectric properties (Fig. 6a). However, the addition of MPS@BT NPs is beneficial for forming β-phase crystals, resulting in high energy loss during energy charging and discharging. Furthermore, nanocomposite networks were built between the MPS@BT NPs and P(VDF-CTFE) to control the size of P(VDF-CTFE) crystals with the help of double-bond creating agents. In this approach, the addition of MPS@BT NPs not only produced an interface between the nanoparticles and the matrix for obtaining a high dielectric constant, but also decreased the size of P(VDF-CTFE) crystals for producing additional interfaces between the crystalline and amorphous phases to attain a high energy density. Most importantly, the cross-linking approach can tailor down the α- and γ-phase crystals, which results in a low ferroelectric loss. Meanwhile, the elastic networks enable the poled polar phase in the smaller ferroelectric crystals to switch back to the paraelectric phase during energy charge and discharge processes, which enhances the reversible behavior of P(VDF-CTFE) crystals for reduced hysteresis as well as low ferroelectric switching loss.

Conclusion

We demonstrated that hierarchical interfaces in P(VDF-CTFE)/MPS@BT ferroelectric nanocomposite networks were modulated by using the cross-linking method, which can achieve unprecedented levels of performance in dielectric capacitor applications. In contrast to BT NPs, the newly structured MPS@BT NPs with double-bonds were embedded and homogeneously dispersed in a cross-linking P(VDF-CTFE) matrix. In this system, hierarchical interfaces in P(VDF-CTFE)/MPS@BT nanocomposite networks were simultaneously modulated by employing double-bond MPS@BT as a cross-linking center. Remarkably, the interfaces between the nanoparticles and the matrix were modulated, and the size of crystalline domains were tailored down at the same time, which leads to producing more additional interfaces between the crystalline and amorphous phases to further enhance energy storage capacitance. More importantly, the cross-linking elastic networks enable the poled polar phase to switch back to its original phase during the energy discharge process, which enhances the reversible behavior of crystalline domains for reduced hysteresis as well as low ferroelectric loss.

With respect to P(VDF-CTFE), the addition of MPS@BT NPs into the nanocomposite networks also regulates the energy discharge rate. The early stage of the discharge process can be accelerated due to the ceramic nanoparticles with a short polarization-retention time. However, the following energy discharge process has obviously been delayed, which is mainly attributed to the fact that the reduced crystalline domains are trapped in the cross-linked matrix. Our systematic study will be useful for developing a novel approach to improve the performance of ferroelectric polymers for electrostatic capacitors.

Experimental

Materials

P(VDF-CTFE) (91/9 mol%) was purchased from Solvay. The Cubic Barium titanate ($BaTiO_3$) nanoparticles (BT NPs) were obtained from Sigma-Aldrich. The size of the BT NPs is about 50 nm. 3-Methacryloxypropyltrimethoxysilane (MPS) was purchased from Ji'nan Guobang Chemical Co., Ltd. The cross-linking agent (benzoyl peroxide, BPO) was obtained from Sinopharma Chemical Reagent Co., Ltd.

Synthesis of MPS@BT NPs

The silane coupling agent MPS was grafted onto the surface of BT NPs. The typical process was as follows: firstly, 20 g of BT NPs was activated by 50 ml of H_2O_2 solution at the reflux temperature of 90 °C for 24 h. Then, the activated BT NPs were centrifuged at 6000 rpm for 5 min and dispersed in distilled water in an ultrasonic bath three times. Secondly, 10 ml of the coupling agent MPS and 5 g of the activated BT NPs were added into 100 ml of a mixed solvent (ethanol and water = 1 : 1), and the contents were magnetically stirred at 90 °C for 24 h. Double bonds were attached chemically on the surface of the activated NPs, forming double-bonds in the MPS@BT NPs, as shown in Fig. 1a.

Preparation of P(VDF-CTFE)/MPS@BT nanocomposite networks by one-pot cross-linking approach

First of all, 0.02, 0.04, and 0.06 g of MPS@BT NPs were added into *N*,*N*-dimethylformamide (DMF) and dispersed by ultrasound for 0.5 hours. Next, 0.4 g of P(VDF-CTFE) powder was added into the solution and stirred at 50 °C to obtain 5 wt%, 10 wt%, and 15 wt% P(VDF-CTFE)/MPS@BT nanocomposites, which were defined as B_5, B_{10}, and B_{15}, respectively.

Furthermore, 0.02, 0.04, 0.06, and 0.08 mg of BPO were subsequently added into 10 wt% B_{10} solutions for preparing 5 wt%, 10 wt%, 15 wt% and 20 wt% cross-linked agent films, which were defined as nanocomposite networks $B_{10}P_5$, $B_{10}P_{10}$, $B_{10}P_{15}$, and $B_{10}P_{20}$, respectively. The final solutions were cast on a Teflon vessel and dried at 60 °C in an air-circulation oven for 48 h, and finally treated in a vacuum oven for 24 h to remove residual solvent. 30 μg of nanocomposite networks were hot-pressed at 200 °C for 1 hour to obtain a high cross-linking degree. The thickness of the films was 30–40 μm.

Characterization

Morphology characterization. The morphology of MPS@BT NPs was studied by using transmission electron microscopy (TEM, JEM-2100); the morphologies of P(VDF-CTFE)/MPS@BT and P(VDF-CTFE)/BT nanocomposites were examined by using a Hitachi S-4800 FE-SEM at the voltage of 5 kV. A cross-section of the nanocomposite was cut off with liquid nitrogen and then sputtered with a layer of gold.

Dielectric and charging/discharging properties. The dielectric properties were recorded as a function of frequency *via* a high-precision LCR meter (HP4284A; Agilent, Palo Alto, CA). The unipolar *P*–*E* loops as well as charging and discharging process were measured using a Radiant Technologies Precision Premier II, which was fitted with 10 kV amplifiers at the testing frequency of 100 Hz. Gold electrodes were prepared on both surfaces of the films for testing.

Fast discharge experiment. The fast discharge rate of nanocomposite networks was measured by a designed capacitor with a charge–discharge system (PK-CPR1502, polyK) at a fixed electric field E by a high-voltage MOSFET switch. The samples were charged under the maximum field strength, and then discharged across a series of load resistors (R_L = 10 kΩ, 100 kΩ, and 3 MΩ). The corresponding capacitance (C) of the samples was measured by using a high-precision LCR meter for the calculation of energy density.

Structure characterization. The structures of P(VDF-CTFE)/MPS@BT nanocomposites (B_5, B_{10}, and N_{15}) and P(VDF-CTFE)/MPS@BT nanocomposite networks ($B_{10}P_5$, $B_{10}P_{10}$, $B_{10}P_{15}$, and $B_{10}P_{20}$) were studied by using X-ray diffraction (XRD, Bruker-D8) and Fourier transform infrared spectroscopy (FTIR, Bruker Tensor) instruments. The XRD curves were collected from 2θ = 10–80° at the speed of 2° min^{-1} with a step interval of 0.02°. The instrument was run at a 35 kV voltage and 30 mA current. FTIR spectra were recorded from 4000 cm^{-1} to 400 cm^{-1}.

The samples were studied by using Solid-state nuclear magnetic resonance (SSNMR, Bruker Advance III HD 400 Spectrometer) at 25 °C operating at a Larmor frequency of 400.2 MHz for ^1H. Direct excitation ^{19}F spectra and 1D $^{19}F\{^1H\}$ cross polarization/magic-angle spinning (CP/MAS) were recorded using a recycle delay of 5 s, and 32 scans.[25] CP experiments with a short CP contact time of 50 μs can eliminate the signal from the amorphous phase. All the spectra were recorded at a MAS frequency of 18 kHz.

Crystallization behavior. The thermal properties of all the samples were measured by using differential scanning calorimetry (DSC 823e, Mettler Toledo). The mass of each sample is about 10 mg. Heat flow curves were recorded under a N_2 atmosphere using a fixed temperature program, which is heating from −50 to 240 °C at a heating rate of 10 °C min^{-1}.

Conflicts of interest

There are no conflicts to declare.

Acknowledgements

This work was supported by the National Natural Science Foundation of China (Grant No. 51703044), the National Key Research and Development Program of China (Grant No. 2017YFA0701301), the School Science Starting Foundation of Hangzhou Dianzi University

(Grant No. KYS205617016), and the Zhejiang Provincial Key Research and Development Program (2019C01121).

References

1 B. J. Chu, X. Zhou, K. L. Ren, B. Neese, M. R. Lin, Q. Wang, F. Bauer and Q. M. Zhang, *Science*, 2006, **313**, 334.
2 Q. Li, L. Chen, M. R. Gadinski, S. Zhang, G. Zhang, H. U. Li, E. Iagodkine, A. Haque, L.-Q. Chen, T. N. Jackson and Q. Wang, *Nature*, 2015, **523**, 576.
3 Y. Zhang, C. Zhang, Y. Feng, T. Zhang, Q. Chen, Q. Chi, L. Liu, G. Li, Y. Cui, X. Wang, Z. Dang and Q. Lei, *Nano Energy*, 2019, **56**, 138.
4 W. Xu, G. Yang, L. Jin, J. Liu, Y. Zhang, Z. Zhang and Z. Jiang, *ACS Appl. Mater. Interfaces*, 2018, **10**, 11233.
5 X. Zhang, Y. Shen, B. Xu, Q. Zhang, L. Gu, J. Jiang, J. Ma, Y. Lin and C.-W. Nan, *Adv. Mater.*, 2016, **28**, 2055.
6 P. Khanchaitit, K. Han, M. R. Gadinski, Q. Li and Q. Wang, *Nat. Commun.*, 2013, **4**, 2845.
7 Y. Chen, L. Yao, C. Yang, L. Zhang, P. Zheng, A. Liu and Q.-D. Shen, *Soft Matter*, 2018, **14**, 7714.
8 P. Michalczyk and M. Bramoulle, *IEEE Trans. Magn.*, 2003, **39**, 362.
9 M. Rabuffi and G. Picci, *IEEE Trans. Plasma Sci.*, 2002, **30**, 1939.
10 J. Li, S. I. Seok, B. Chu, F. Dogan, Q. Zhang and Q. Wang, *Adv. Mater.*, 2009, **21**, 217.
11 Y. Li, X. Huang, Z. Hu, P. Jiang, S. Li and T. Tanaka, *ACS Appl. Mater. Interfaces*, 2011, **3**, 4396.
12 R. Gregorio, M. Cestari and F. E. Bernardino, *J. Mater. Sci.*, 1996, **31**, 2925.
13 H. Tang, Y. Lin, C. Andrews and H. A. Sodano, *Nanotechnology*, 2010, **22**, 015702.
14 Q. Li, K. Han, M. R. Gadinski, G. Zhang and Q. Wang, *Adv. Mater.*, 2014, **26**, 6244.
15 Z. Pan, L. Yao, J. Zhai, D. Fu, B. Shen and H. Wang, *ACS Appl. Mater. Interfaces*, 2017, **9**, 4024.
16 H. Tang and H. A. Sodano, *Nano Lett.*, 2013, **13**, 1373.
17 P. Kim, S. C. Jones, P. J. Hotchkiss, J. N. Haddock, B. Kippelen, S. R. Marder and J. W. Perry, *Adv. Mater.*, 2007, **19**, 1001.
18 Y. Chen, X. Tang, J. Shu, X. Wang, W. Hu and Q.-D. Shen, *J. Polym. Sci., Part B: Polym. Phys.*, 2016, **54**, 1160.
19 X. Huang and P. Jiang, *Adv. Mater.*, 2015, **27**, 546.
20 L. Xie, X. Huang, Y. Huang, K. Yang and P. Jiang, *J. Phys. Chem. C*, 2013, **117**, 22525.
21 L. Xie, X. Huang, C. Wu and P. Jiang, *J. Mater. Chem.*, 2011, **21**, 5897.
22 S. Liu, S. Xue, B. Shen and J. Zhai, *Appl. Phys. Lett.*, 2015, **107**, 032907.
23 Z. Zhang and T. C. M. Chung, *Macromolecules*, 2007, **40**, 783.
24 W. Xia, Z. Xu, F. Wen, W. Li and Z. Zhang, *Appl. Phys. Lett.*, 2010, **97**, 222905.
25 F. X. Guan, L. Yang, J. Wang, B. Guan, K. Han, Q. Wang and L. Zhu, *Adv. Funct. Mater.*, 2011, **21**, 3176.
26 J. Li, S. Tan, S. Ding, H. Li, L. Yang and Z. Zhang, *J. Mater. Chem.*, 2012, **22**, 23468.
27 Y. Chen, Z. Cheng and Q. Shen, *IEEE Trans. Dielectr. Electr. Insul.*, 2017, **24**, 682.
28 X.-Z. Chen, Z.-W. Li, Z.-X. Cheng, J.-Z. Zhang, Q.-D. Shen, H.-X. Ge and H.-T. Li, *Macromol. Rapid Commun.*, 2011, **32**, 94.
29 Y. Huang, J.-Z. Xu, T. Soulestin, F. D. Dos Santos, R. Li, M. Fukuto, J. Lei, G.-J. Zhong, Z.-M. Li, Y. Li and L. Zhu, *Macromolecules*, 2018, **51**, 5460.
30 Y. Wang, X. Zhou, Q. Chen, B. Chu and Q. Zhang, *IEEE Trans. Dielectr. Electr. Insul.*, 2010, **17**, 1036.
31 B. Gao, Y. Chen and J. Men, *J. Chromatogr. A*, 2011, **1218**, 5441.
32 X. Zhu, J. Zhu, S. Zhou, Z. Liu and N. Ming, *J. Cryst. Growth*, 2008, **310**, 434.
33 P. Ren, H. Fan, X. Wang and K. Liu, *Mater. Lett.*, 2011, **65**, 212.
34 D. Wang, Y. Bao, J.-W. Zha, J. Zhao, Z.-M. Dang and G.-H. Hu, *ACS Appl. Mater. Interfaces*, 2012, **4**, 6273.
35 F. Liu, Q. Li, Z. Li, Y. Liu, L. Dong, C. Xiong and Q. Wang, *Compos. Sci. Technol.*, 2017, **142**, 139.
36 J. W. Park, Y. A. Seo, I. Kim, C. S. Ha, K. Aimi and S. J. Ando, *Macromolecules*, 2004, **37**, 429–436.